SPATIOTEMPORAL CHARACTERIZATION OF LAND SURFACE TEMPERATURE IN RELATION LANDUSE/COVER: A SPATIAL AUTOCORRELATION APPROACH

DIKSHA[1], MAYA KUMARI[1*], RINA KUMARI[2]

[1]*Amity School of Natural Resources & Sustainable Development, Amity University Uttar Pradesh, Noida, Sector 125. India*
[2]*School of Environment and Sustainable Development, Central University of Gujarat, Sector 30, Gandhinagar, India*
Corresponding author email: maya.84s@gmail.com

ABSTRACT

The land use and land cover (LULC) characteristics of Ghaziabad have experienced dynamic changes because of the city's ongoing industrialization and urbanisation processes. These shifts can be directly attributed to human actions. These shifts can be directly attributed to human actions. Thermal variation in the study area necessitates LULC analysis. Landsat and Sentinel satellite data for 2011 and 2021 were used to map LULC, estimate land surface temperature (LST) and analysis spatial autocorrelation among the variables using ArcGIS software and the Google Earth Engine (GEE) cloud platform. A sharp descent is observed in the cropland while built-up area has increased during the study period. With the increase in the built-up surface in the area, the ambient temperatures have also increased from 18.70 °C in 2011 to 21.81 °C in 2021 leading to urban heat island effect. At all spatial scales, spatial autocorrelation is a characteristic property of most ecological parameters. The spatial clustering of LST in an ecosystem can play a crucial role in determining the dynamics of LULC. The Moran's, I show that there is a considerable level of spatial autocorrelation in the values of LST and highly clustered pattern for both the years. Monitoring and understanding the surface thermal environment is crucial to discerning the causes of climate change.

Keywords: Land use land cover; Land Surface Temperature; spatial autocorrelation; Ghaziabad

INTRODUCTION

Rural migration and the industrialization process have accelerated the urbanisation process since the 18th century, resulting in an unchecked increase in the population in the urban areas globally (Chau *et al*., 2021; Subasinghe *et al*., 2016). According to the United Nations Division's World Urbanization Prospects report, urbanisation has surpassed ruralisation on a worldwide scale (Nations *et al*., 2019). According to the 2011 census, out of the 1.21 billion Indians, 833 million (or 80 %) reside in rural areas, while 377 million do so in urban areas

(Sarkar, 2020). The growth of cities has a profound impact on the natural biophysical environment because it results in significant shifts in land use and land cover (LULC) (Das & Angadi, 2020). The thermal behaviour of the terrain is influenced by the surface LULC, removal of vegetation cover and increased urban activity also affects the regional climate (Kaiser *et al*., 2022; Park *et al*., 2022). The energy transfer between the earth's surface and the atmosphere, as well as between the earth's surface and the biosphere, is measured by the Land Surface Temperature (LST) (Moazzam *et al*., 2022). The temperature and humidity of the air as well as the speed and direction of the wind changes because of the modification of the LULC (Li *et al.,* 2018). In this way, the area develops its own urban climate as a result of regional climate changes and local environment of the area creates a superficial urban heat island (Masson *et al*., 2020). In urban areas, mainly due to the reflection from concrete structures, there is an increase in LST and the consequent formation of heat pockets (Islam *et al*., 2022). Vegetation absorbs and reflects solar radiation controlling the exchange of latent heat, which in turn affects the LST (Duveiller *et al*., 2018). Therefore, a decrease in vegetation causes increase in the LST (Bhatt & Hossain, 2019). In urban areas, a temperature correlation can be seen between the higher and lower temperature zones. Remote sensing techniques can be used to observe and study such correlations (Kumari *et al*., 2019). In the last decade, some studies have been conducted in major Indian cities like Mumbai, Kolkata, Ahmedabad and Delhi to find out the relationship between LULC and LST (Aithal *et al*., 2019). The impact of urbanization, LULC changes, and decadal impacts of LULC on LST were also observed in some large urban districts and cities (Gohain *et al*., 2021; Shaikh *et al.*, 2021). A wide range of methodologies have been applied in various research to gain an understanding of the connection that exists between the LST of a region and the land use of that region (Hu *et al*., 2021; Stewart & Nitschke, 2017). Observing temperature at meteorological stations is the conventional method of studying the thermal climate. Previously, LST was calculated for a few points or locations, and the temperature data were then interpolated. But now high resolution and freely available satellite imagery can be used to estimate LST and various Geographic Information System (GIS) softwares and cloud platforms allow us to create maps (Almeida *et al*., 2021). Various types of thermal and optical bands from satellite imagery like MODIS, Landsat, Sentinel are available with different spatial and temporal resolutions to calculate LST and create LULC maps (Chaves *et al*., 2020). GIS software offers spatial statistics tools such as Spatial Autocorrelation that help analyse the distribution and relationship of geographic features (Bao *et al*., 2000; Yan *et al*., 2021). Therefore, remote sensing can be utilised to investigate temperature increases at the surface as well as their general trends of either their increase or decrease. To gain a deeper comprehension of how the spatial processes of the environment function in the world, it is necessary to study spatial patterns. Hence, the hypothesis of the present study is that there is no relationship between the variation of LST and LULC and both are also not spatial autocorrelated.

METHODOLOGY AND DATA USED

Ghaziabad District: Study Area

Ghaziabad district of Uttar Pradesh is an important and popular district in NCR region of India (Figure 1). This district covers an area of an approximately 1980.69 km^2 and is located at 28.7892° N latitude and 77.5161° E longitude. It touches the borders of the capital and is an important industrial and commercial centre for Delhi. The district is divided into eight development blocks and four tehsils. The rivers Yamuna and Ganga, as well as their

tributaries Hindon and Kali, drain the district of Ghaziabad. Almost half of the district is irrigated by means of minor irrigation structures including tube wells, capacity wells, and surface irrigation canals. The Hindon River flows out of the district and is the main source of water for the district. The Ganga and Yamuna rivers touch the boundaries of the district.

- **Climate and Rainfall-** About 80 to 85 % of the annual precipitation falls between July and September, mainly due to the southwest monsoon, with 15 to 20 % of the remaining precipitation falls between January and March. The average annual rainfall in the district is 764 mm. Both summer and winter in the district are extreme, with temperatures rising up to 40 °C in midsummer and falling to 5 °C in January. Winter lasts from November to February and Summer lasts from April to mid-June.

- **Soil types and Geomorphology-** The Ganga River forms the eastern boundary of the entire Ghaziabad district while the Yamuna River defines the western boundary. The region almost resembles a flat, monotonous plain that has been divided by drainage of different orders. The Ghaziabad district is practically situated on the former floodplain of the Hindon river. Morphologically speaking, the region can be broken up into three distinct morpho units: an older alluvial plain, an older flood plain, and an active flood plain. River banks are rocky and precipitous. The older alluvium covers the entire upland and interfluve region between the main Yamuna and Hindon and Hindon and Ganga drainage routes. Different erosional and depositional agencies can give insight into soil development in the district. There are a variety of soils, ranging from sand to stiff clays. Bhur is the name given to pure sand. Clay is known as Matiyar. Agricultural soils that contain equal portions of sand and clay are referred to as dumat or loam.

Fig. 1: Study area, Ghaziabad district
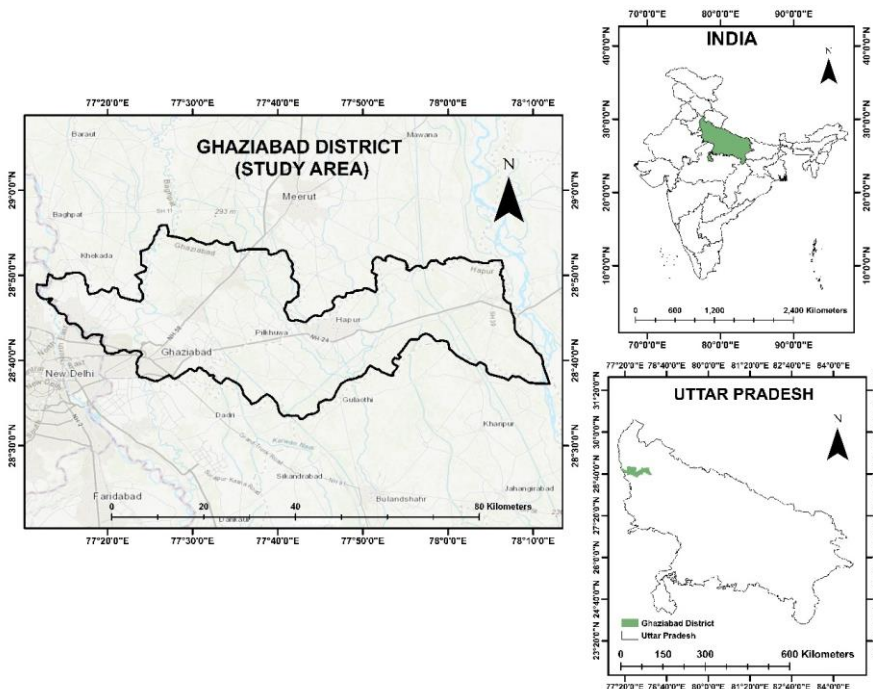
Data used

For the LULC classification and the LST derivation, the imageries from Landsat 7, Landsat 8, and Sentinel 2 from the years 2011 and 2021 for the month of February served as the primary data. On the cloud platform that GEE offers, the LULC categorization was completed, and ArcMap was used to calculate the LST. Table 1 lists the satellite data that were used in this study.

Table 1: Summary of satellite data

Data sets	Month and Year of acquisition	Cloud cover	Spatial resolution	Temporal resolution
Landsat 7 ETM+	February 2011	less than 10%	30 Metre	16 Days
Landsat 8 TIRS	February 2011	less than 10%	30 Metre	16 Days
Sentinel 2	February 2021	less than 10%	10 Metre	5 days revised time

METHODOLOGY

General LULC mapping procedures in the GEE environment

Landsat 7 and Sentinel 2 satellite data were used for the LULC classification. Several phases were used to create the LULC map in GEE: data selection, data pre-processing, selection of training samples, classification, and error matrix (Figure 2). The satellite images of the month of February have been selected. Additionally, pixels with clouds and scanline errors were masked using a Java script in GEE. While images may have overlapping pixels, the median of each band was computed separately. The pre-processed images were classified using the supervised classification method, which also defines the land cover categories, using the signatures from the training samples. Urban, built-up, cropland, water bodies, green cover, fallow land, and barren land were selected as different land cover units, since the classes were determined by visual interpretation of satellite imagery. There were three different spectral bands that were employed for the class-visual interpretation (red, green, and near infrared). In GEE, supervised classification was carried out using the Classification and Regression Tree (CART) classifier. As a result, after running the script, two classified images were obtained. Most of the spectral bands were used as inputs into the classification process, in order to get the desired result. These included the four visible and near-infrared bands as well as the two-short-wave infrared (SWIR) bands. The overall accuracy was determined by using the error matrix.

LST calculations

Space-based remote sensing data from Landsat satellites have been continuously available for more than four decades. For this study, Landsat 7 and 8 series were used. Clear sky Landsat satellite images were collected for two years 2011 and 2021 to calculate LST in Ghaziabad district. The USGS Earth Explorer website offers free Landsat data downloads. Landsat 7 ETM+ contains a thermal infrared (TIR) band in addition to six reflective bands with a 30 m spatial resolution. The spatial resolution of the thermal band is 120 m for TM and 60 m for ETM+, but USGS offers it at 30 m after cubic convolution resampling. Landsat 8 images have a spatial resolution of 30 m. The OLI sensor has nine reflective bands and there are two TIR bands on the Landsat 8 TIRS sensor (band 10 and band 11). The USGS resampled and published these thermal bands with a resolution of 30 m, despite their original

spatial resolution of 100 m. LST was calculated with the LANDSAT 7 and 8 Science Data Users Handbook by using raster calculator in ArcMap 10.8.

The following formulas were used to calculate LST based on data from Landsat 8:
- **The top of the atmospheric spectral radiation**

The algorithm commences with the input of band 10. The spectral radiance was calculated using the raster calculator by using the formula shown in equation 1.

$$L\lambda = M_L * Q_{cal} + A_L - O_i \qquad\qquad 1$$

Where

M_L = multiplicative rescaling factor for each band.
Q_{cal} = is band 10.
A_L = represents band-specific rescaling factor.
O_i = Correction (Band 10)

- **Radiance to At-Sensor Temperature Conversion**

The TIRS band data must be converted from spectral radiance to brightness temperature using the thermal constants in the metadata file (BT). To convert reflectance to BT, use equation 2.

$$BT = \frac{K_2}{\ln[(K_1/L\lambda) + 1]} - 273.15 \qquad\qquad 2$$

Where

K_1 = The metadata values for the thermal conversion constants.
K_2 = Constants for thermal conversion taken from the metadata.
Radiant temperature was yielded by essentially adding absolute zero to get the results in Celsius. $(-273.15\ °C)$.

- **NDVI to Correct Emissivity**

Landsat visible and near-infrared bands were used to calculate NDVI. The quantity of vegetation is a key element, the NDVI can be used to estimate general vegetation conditions. The amount of vegetation must be calculated after the NDVI since it is closely related to both the NDVI and emissivity, which is related to P_V.

$$NDVI = \frac{NIR(band\ 5) - R(band\ 4)}{NIR(band\ 5) + R(band\ 4)} \qquad\qquad 3$$

Where
NIR= Near-infrared Band.
R= Red Band.

- **Calculating the Vegetation Proportion**

P_V was calculated using the global NDVI values for vegetation and soil (NDVI = 0.5 and NDVI = 0.2) for global conditions. Because NDVI values vary from place to place, the 0.5 NDVI estimate for vegetated surfaces may be too low. Since $NDVI_V$ and $NDVI_S$ rely on atmospheric conditions, at-surface reflectivity's can be used to determine global values of NDVI, but TOA reflectivity's cannot. Equation 4 was used to calculate P_V.

$$P_v = \left(\frac{\text{NDVI} - \text{NDVI}_s}{\text{NDVI}_v - \text{NDVI}_s}\right)^2 \qquad\qquad 4$$

- **Land Surface Emissivity (LSE)**

To determine LST, one must first calculate the LSE, which is the efficiency with which thermal energy is transmitted from the surface into the atmosphere and is expressed as a proportionality factor. The ground emissivity was conditionally estimated using Equation 5.

$$\varepsilon_\lambda = \varepsilon_{v\lambda} P_v + \varepsilon_{s\lambda}(1 - P_v) + C_\lambda \qquad\qquad 5$$

Where

ε_λ = Vegetation and soil emissivity.
ε_s = Vegetation and soil emissivity.
C = Surface roughness.

The equation 6, along with the values for the emissivity constants, can be used to express the condition.

$$\varepsilon_\lambda = \begin{cases} \varepsilon_{s\lambda}; & \text{NDVI} < \text{NDVI}_s \\ \varepsilon_{v\lambda} P_v + \varepsilon_{s\lambda}(1 - P_v) + C; & \text{NDVI}_s \leq \text{NDVI} \leq \text{NDVI}_v \\ \varepsilon_{s\lambda} + C; & \text{NDVI} > \text{NDVI}_v \end{cases} \qquad 6$$

When the NDVI is less than 0, it is considered to be water, and an emissivity value of 0.991 is given. The NDVI value between 0 and 0.2, which shows soil coverage, is given the emissivity value of 0.996. For values between 0.2 and 0.5, soil and vegetation cover are considered a mixture, and equation 6 is applied to obtain the emissivity. NDVI values greater than 0.5 are regarded as representing vegetation cover.

- **Land Surface Temperature**

The final step of extracting the LST, or the emissivity corrected LST, was calculated using equations 7 and 8.

$$T_s = \frac{BT}{\left\{1 + \left[\left(\frac{\lambda BT}{p}\right) In\varepsilon_\lambda\right]\right\}} \qquad\qquad 7$$

$$\rho = h\frac{c}{\sigma} = 1.438 \times 10^{-2}\ \text{mK} \qquad\qquad 8$$

Where

T_s = LST in degrees Celsius.
BT = Brightness temperature.
λ = Average wavelength of Landsat 8 image, band 10
p = [h × (c/σ)] = 1.438 x 10-2 mK
h = 6.62607004 × 10-34 m2 kg / s (Planck's constant)
c = Speed of light ~ 3.00×108 m/s
σ = 1.38064852 × 10-23 m2 kg s-2 K-1 (Boltzmann Constant)

The LANDSAT 7 Science Data Users Handbook was used to derive LST.

- **Spectral Radiance**

Equation 9 was used to calculate the spectral Radiance (L) from the pixel value of the thermal band of the satellite image.

$$L_\lambda = Gain \; X \; DN \; + \; offset \qquad\qquad 9$$

Where
$L\lambda$ = Spectral radiance.
DN = Value of a given pixel.
$Gain$= Values from metadata.
$f\,set$= Values derived from metadata

- **Surface temperature**

The temperature in Kelvin was calculated from the spectral radiance. The conversion formula is given in equation 10.

$$T_B = \frac{K2}{In\left(\frac{K1}{L_\lambda} + 1\right)} \qquad\qquad 10$$

Where
T_B= Surface temperature in kelvin.
$K1$= Constant value (666.09)
$K2$= Constant value (1282.71)
L_λ= Spectral radiance calculated from equation 9.

- **Land surface temperature**

Using equation 11, the Land Surface Temperature (LST) was computed.

$$LST = \frac{T_B}{1 + \left(\frac{\lambda T_B}{P}\right) In\epsilon} \qquad\qquad 11$$

Where
T_B= Surface temperature calculated from equation 10.
λ= Wavelength of the emitted radiance.
P= h X c/σ (1.438 X 10-2 Mk).
σ= Boltzmann's constant (1.38 x 10-23JK-1).
h= Planck's constant (6.626 x 10-34Js).
h= Velocity of light (2.998 x 108ms-1).

Spatial autocorrelation

One of the most well-known and widely used spatial autocorrelation measures is the Moran's Index (I), which Moran first introduced in 1948. The Spatial Autocorrelation (Global Moran's I) tool computes spatial autocorrelation by simultaneously calculating feature locations and feature values. It determines whether the pattern expressed is clustered, scattered, or random in the presence of a collection of features and an associated attribute. To determine its applicability, the tool computes the Moran's I Index value, as well as a z-score, p-value, and other metrics.   It is calculated by using equation 12 given below.

$$I = \frac{n}{S_0} \; \frac{\sum_{x=1}^{n} \sum_{y=1}^{n} w_{x,y} z_x z_y}{\sum_{x=1}^{n} z_x^2} \qquad\qquad 12$$

Where
z_x = Deviation of an attribute from its mean (xi - $\overline{X}$) for feature X.
w_{xy} = Spatial weight between features X and Y.
n = Total number of features.
S_0 = Sum of all spatial weights.

$$S_0 = \sum_{x=1}^{n} \sum_{y=1}^{n} w_{x,y}$$ 13

The statistics yield z_j score, is given by -

$$z_x = \frac{I - E[I]}{\sqrt{V[I]}}$$ 14

Where

$$E[I] = -1/_{(n-1)}$$ 15

$$V[I] = E[I^2] - E[I]^2$$ 16

Above is a mathematical explanation of the Global Moran's I statistic. The ArcMap Spatial Autocorrelation Moran's Index (I) tool used in this study to determine the mean and variance for the attribute under consideration. The Moran's Index ranges from +1 to -1. If 'I' equal +1, this implies that the observed pattern is spatially clustered. 'I' equal -1, on the other hand, means spread or dispersion. 'I' assigns a point value of almost zero or equivalent to the lack of autocorrelation. Only after considering the z-score and the p-value of the index, final conclusions are drawn regarding the observed pattern.

Fig 2: Methodology flow chart
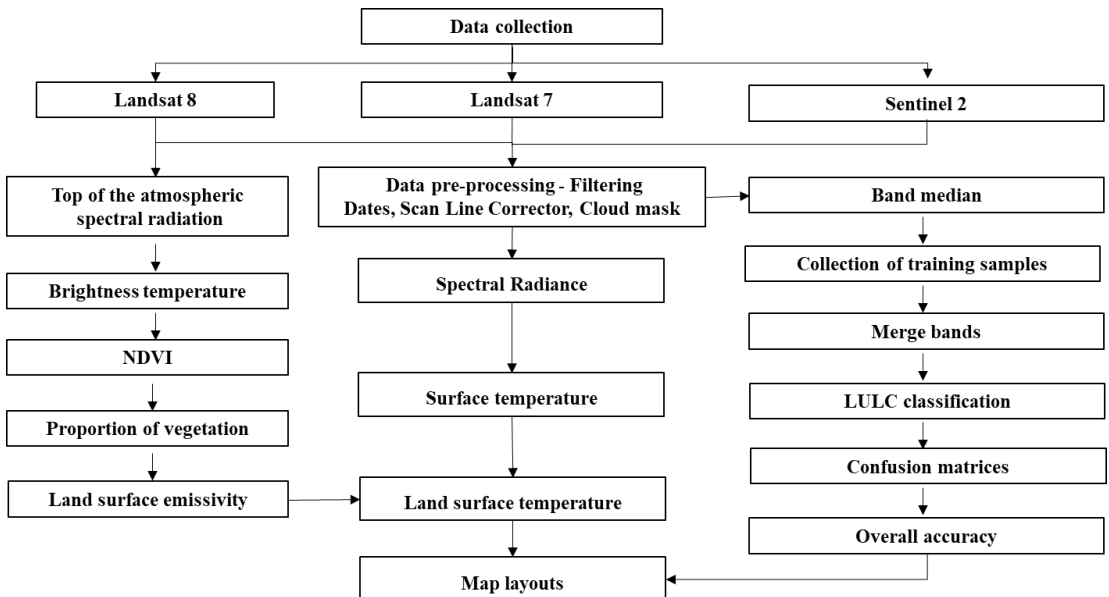
RESULTS

Land use land cover (LULC) Maps

The study area consists of six classes viz., Urban and Built-up; Water bodies; cropland; Barren land; Fallow land and green cover.

In 2011, cropland comprised 59 percent of the entire study region, stretching from the east to the northwest (Figure 3). It has steadily decreased to 46 percent of the total area in 2021 (Table 2). The decline can be attributed to the conversion of cropland to other uses, such as small mango gardens and construction activities.

Fig. 3: Classification of land use and land cover for the years 2011 and 2021
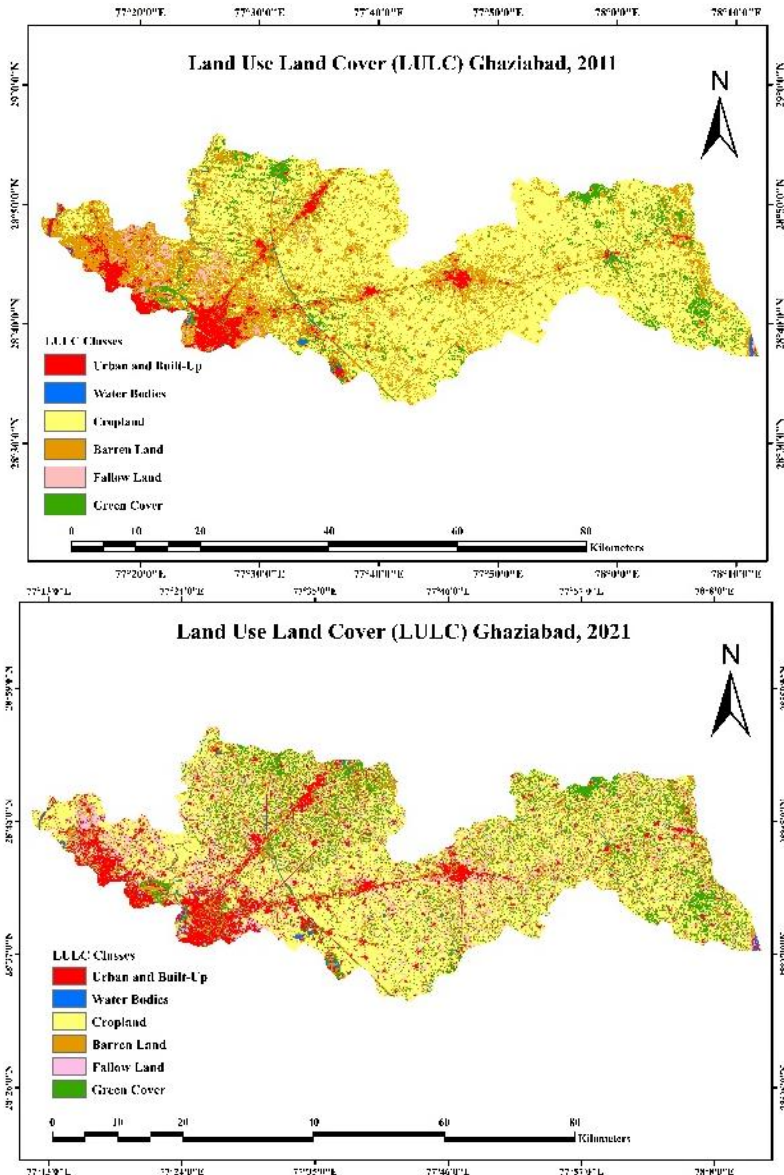
Table 2: Changing trends of LULC classes according to area

LULC Classes	Area (km²) 2011	Area (km²) 2021	Area (%) 2011	Area (%) 2021	Change	
Urban and Built-Up	109.25	241.04	6%	12%	6%	Increased
Water Bodies	18.11	12.91	1%	1%	0%	Constant
Cropland	1160.00	900.34	59%	46%	13%	Decreased
Barren Land	514.51	289.69	26%	15%	11%	Decreased
Fallow Land	43.38	267.50	2%	14%	12%	Increased
Green Cover	135.41	269.18	7%	14%	7%	Increased
Total	1980.69	1980.69	100%	100%		

The development of Large-scale establishment of companies, institutions, and structures is what has caused a transition away from agricultural use. Under similar physical and environmental conditions, cropland is a diverse type of green cover. Green cover has increased from 7 to 14 percent due to the diversion of cropland cover to other uses. Similarly urban and built-up areas nearly doubled while the water bodies occupying least percent of LULC remains constant over the decade.

Fig. 4: Area of LULC classes in km²
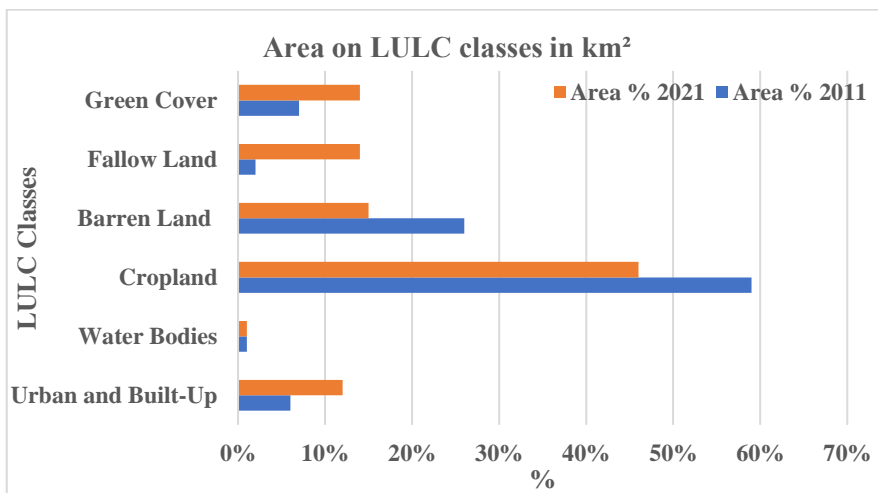
Classification Accuracy Assessment

The final phase of the classification process is called accuracy assessment, and it is one of the most critical steps (Tassi & Vizzari, 2020). The objective of the accuracy assessment is to make a numeric evaluation of the degree to which the pixels were correctly sampled into the appropriate land cover groups (Qu *et al*., 2021). In addition, locations that could be easily recognised on high-resolution images from Landsat and Sentinel as well as satellite data and the terrain map in GEE were used for the accuracy assessment pixel selection. This was the primary focus of the main attention for the pixel selection. Within the restricted view of the study area, a total of two hundred and fifty-four validation points were captured. The

Accuracy Assessment Cell Array Reference column was populated with data corresponding to the best possible deduction for each reference point.

Table 3: Classis wise accuracy assessment statistical parameters 2011

validation error matrix 2011						
LULC Classes	**6 Elements**					
Urban and Built-Up	15	0	0	0	0	0
Water Bodies	0	0	0	0	0	0
Cropland	0	0	10	0	0	0
Barren Land	0	0	2	9	0	0
Fallow Land	1	0	0	2	12	0
Green Cover	0	0	1	0	0	13
validation overall accuracy:	**0.92**					

The accuracy analysis concludes that the 2011 LULC images have a validation overall accuracy of 0.92, while the 2021 LULC images have a validation overall accuracy of 0.8. (Table 3 and 4).

Table 4: Classis wise accuracy assessment statistical parameters 2021

validation error matrix 2021						
LULC Classes	**6 Elements**					
Urban and Built-Up	0	0	0	0	0	0
Water Bodies	27	22	0	1	3	0
Cropland	0	0	32	0	0	0
Barren Land	0	0	0	19	0	1
Fallow Land	1	0	0	0	21	0
Green Cover	0	0	0	0	0	38
validation overall accuracy:	**0.8**					

Land surface temperature (LST) Maps

The advantage of geospatial technology allows us to calculate the LST using the thermal bands (Rosado *et al.,* 2020). The LST ranged from 12.71 °C to 29.30 °C in February 2011 (Figure 5 and 6), with an average temperature of 18.70 °C. The mean LST in 2021 was 21.81 °C, with a minimum LST of 16.51 °C and a maximum LST of 42.74 °C.

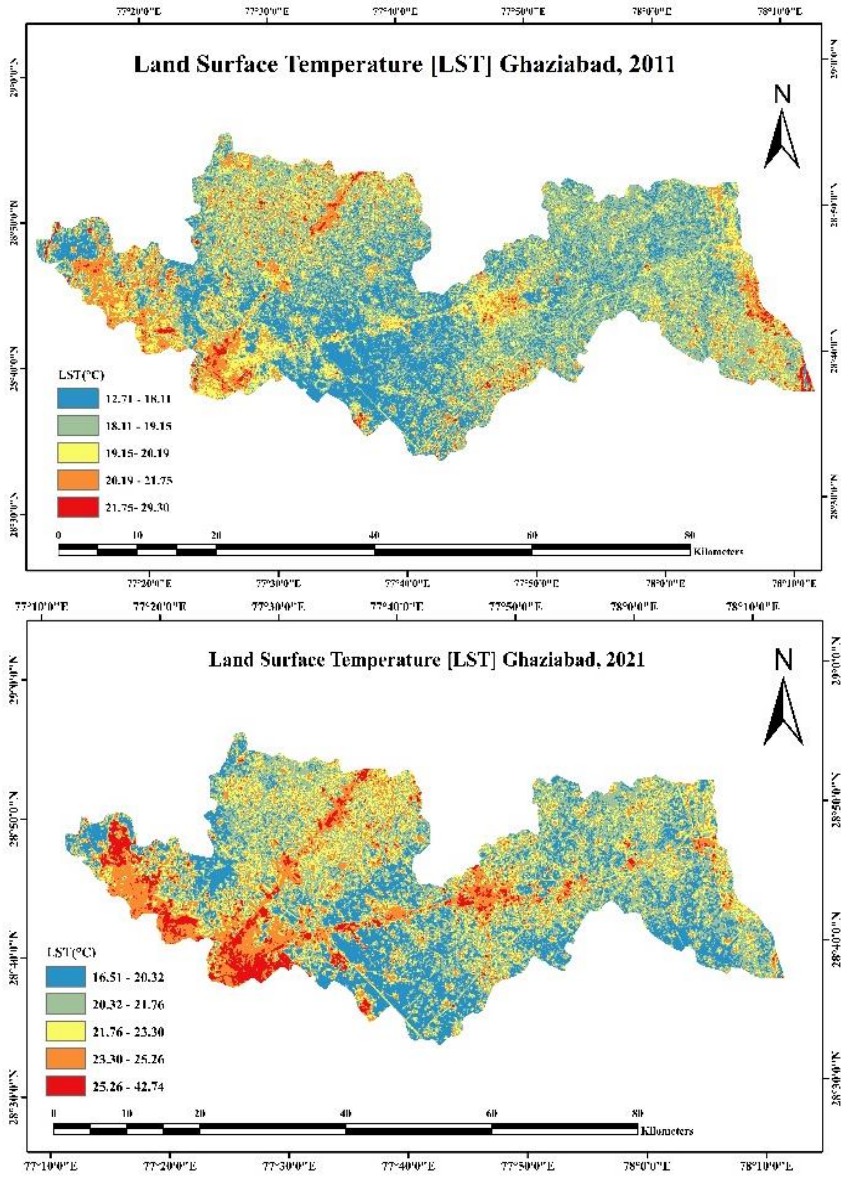**Fig. 5: Land surface temperature in the Ghaziabad district in both 2011 and 2021**
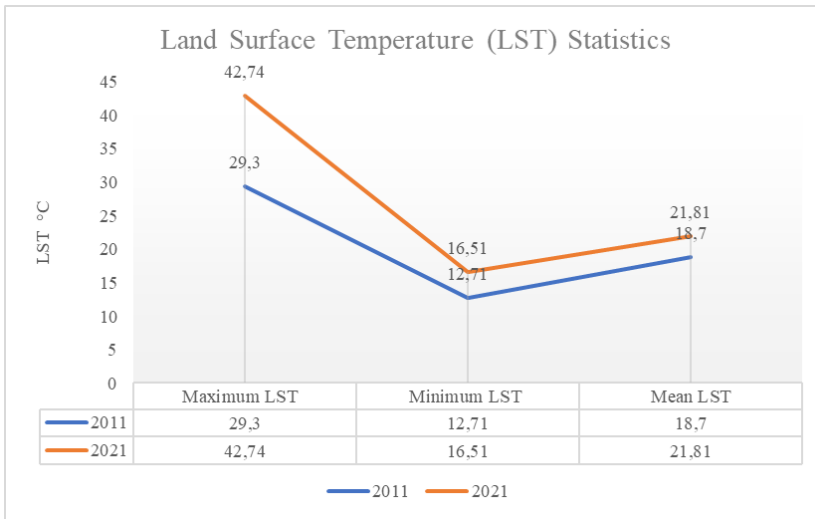
Fig. 6: LST Statistics During the Time Period Under Study

Land Surface Temperature (LST) Statistics

	Maximum LST	Minimum LST	Mean LST
2011	29,3	12,71	18,7
2021	42,74	16,51	21,81

Spatial Autocorrelation: Spatial Variation in a Variable

The Global Moran's Index values for 2011 and 2021 are greater than zero, indicating the possibility of either a strongly clustered pattern or positive autocorrelation (Table 5 and Figure 7).

Fig. 7: Spatial Autocorrelation clustered pattern
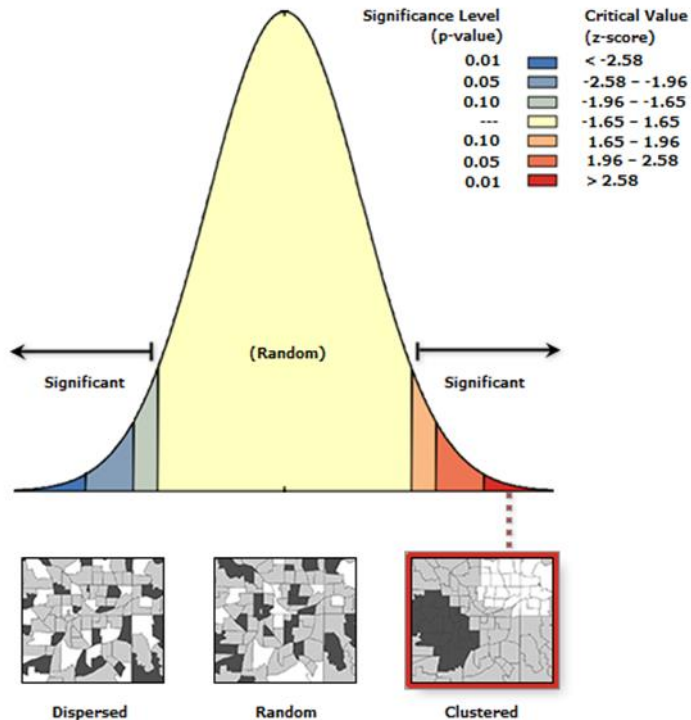
Examining the p values confirms the same. For both the years computed p value is less than 0.05 ($p \leq 0.05$), disproving the fundamental presumption of independence and randomness in the data values. Because the obtained z-score is greater than 2.58 (z-score > 2.58) for both the years, there is less than a 1% chance that the observed pattern is the result of a stochastic process.

Table 5: Analysis of Spatial and Temporal Clusters

Year	Moran's Index	z-score	p value
2011	0.33	22.20	0.00
2021	0.52	33.94	0.00

DISCUSSION

LULC analysis

In recent decades, urban areas have experienced rapid population growth, with that growth being significantly higher than that of rural areas. The reason for this is due to the fact that metropolitan areas are the epicentres of economic activity and the hubs of transportation (Horo & Punia, 2019). The conversion of the land cover into barren land during 2011 could be the result of construction activities, skyscrapers, and residential buildings, while in 2021 it may be urbanized and built-up. The rapid increase in the area used for non-agricultural purposes, the area used for tree crops and groves, as well as the area used for fallow lands, may be the cause of the falling trend in these types of land (Naikoo *et al*., 2020). Additionally, fallow land grew by 12 percent in 2021, climate change being the main contributor. Monsoon instability, pricey diesel irrigation systems, and land fragmentation (motto: nuclear-style families) are all raising the expense of cultivation. Given the steadily shrinking net planted area, it is currently a very difficult issue for policymakers to maximise the revenue of the farming community. Due to the demand for water to meet the population's basic needs, water bodies are slightly declining in a decade (Figure 4).

LST analysis

There is an increase of 3.11 degree Celsius in the average LST values between 2011 and 2021 in the study area. The construction of new buildings, industries, and other forms of urban development contributed to the rise in temperature that occurred in the year 2021. Relationship between LST and LULC has the strongest correlation (Guha *et al.,* 2020). Most of the solar energy that is absorbed by the land is altered by human activities such as construction and modification of the landcover. Because of their superior insulation and capacity to keep heat in, this results in higher temperatures and less evaporative cooling than would otherwise be the case. Higher LST values were related with industrial and built-up areas, and vice versa for green cover and waterbodies. Green cover and waterbodies related to lower LST values. The highest temperatures were found in urban and suburban regions with bare soil, whereas the lowest temperatures were found in green cover areas such as parks (Figure 5). The changes in land use have a significant impact on the temperature pattern that exists in the study area. In contrast to the other types of terrain, such as built-up regions, the temperature was significantly lower in the croplands and the green cover. The built-up or suburban area that has little to no green cover tends to have LST values that are relatively higher. Since majority of the people moves to Ghaziabad in search of employment

opportunities, the residential area has expanded in the past decade along with the LST, as was mentioned earlier, Ghaziabad is situated in the National Capital Region (NCR), and the district is also recognised as an industrial hub. As a result, Land Use (LU) planners, will be able to reduce the rising LST caused by changes in LULC by using the potential findings (Rehman *et al.*, 2022).

Spatial Autocorrelation analysis

A strongly clustered pattern or positive autocorrelation is observed for both the years. Solar radiation reacts and interacts with LULC characteristics to produce a positive spatial autocorrelation with clustered patterns. The concept of spatial autocorrelation can also be applied to a variety of other studies, such as assessing the spatial pattern of forest litter carbon (FLC) density in southeast China using spatial autocorrelation and Global Moran's I statistic (Fu *et al.,* 2014). They discovered a significant positive spatial correlation between FLC density. Another study discovered that the spatial clustering of LST in an ecosystem can be used to evaluate LULC dynamics. According to Moran's I, LST values in built-up areas are highly clustered or exhibit a high degree of positive spatial autocorrelation (Kumari *et al.*, 2019).

CONCLUSION

In the current study, a spatio-temporal analysis for LULC and LST was performed for the two years 2011 and 2021. The LST was derived, in accordance with the LANDSAT 7 and 8 science data user guides indicated that the surface temperature has significantly risen with an average temperature of 3.11 °C over time because of urbanisation and other human-caused activities. The results indicated that the LST is likely to be influenced by land use type. The building material has a positive synergetic relationship with LST and an inverse correlation with the amount of vegetation. The LST values calculated for the decade also indicated a moderate degree of spatial dependence. In addition, Moran's, I Index which is an effective tool for examining the spatial patterns of environmental and biological factors in a metropolitan ecosystem indicated that spatial patterns corresponded with spatial clusters. It is important for the Ghaziabad municipality to take should proactively steps, including as urban planning, building pattern management and tree planting for sustainable urban ecosystem.

CONFLICTS OF INTEREST

The authors declare no conflict of interest.

REFERENCES

Aithal, B. H., M C, C., & G, N. (2019). Assessing land surface temperature and land use change through spatio-temporal analysis: a case study of select major cities of India. *Arabian Journal of Geosciences*, *12*(11), 367. https://doi.org/10.1007/s12517-019-4547-1

Almeida, C. R. de, Teodoro, A. C., & Gonçalves, A. (2021). Study of the Urban Heat Island (UHI) Using Remote Sensing Data/Techniques: A Systematic Review. *Environments*, *8*(10), 105. https://doi.org/10.3390/environments8100105

Bao, S., Anselin, L., Martin, D., & Stralberg, D. (2000). Seamless integration of spatial

statistics and GIS: The S-PLUS for ArcView and the S+Grassland Links. *Journal of Geographical Systems*, *2*(3), 287–306. https://doi.org/10.1007/PL00011459

Bhatt, R., & Hossain, A. (2019). Concept and Consequence of Evapotranspiration for Sustainable Crop Production in the Era of Climate Change. In *Advanced Evapotranspiration Methods and Applications* (pp. 95–106). IntechOpen. https://doi.org/10.5772/intechopen.83707

Chau, K., Franklin, M., Lee, H., Garay, M., & Kalashnikova, O. (2021). Temporal and Spatial Autocorrelation as Determinants of Regional AOD-PM2.5 Model Performance in the Middle East. *Remote Sensing 2021, Vol. 13, Page 3790*, *13*(18), 3790. https://doi.org/10.3390/RS13183790

Das, S., & Angadi, D. P. (2020). Land use-land cover (LULC) transformation and its relation with land surface temperature changes: A case study of Barrackpore Subdivision, West Bengal, India. *Remote Sensing Applications: Society and Environment*, *19*, 100322. https://doi.org/10.1016/j.rsase.2020.100322

Duveiller, G., Hooker, J., & Cescatti, A. (2018). The mark of vegetation change on Earth's surface energy balance. *Nature Communications*, *9*(1), 679. https://doi.org/10.1038/s41467-017-02810-8

E. D. Chaves, M., C. A. Picoli, M., & D. Sanches, I. (2020). Recent Applications of Landsat 8/OLI and Sentinel-2/MSI for Land Use and Land Cover Mapping: A Systematic Review. *Remote Sensing*, *12*(18), 3062. https://doi.org/10.3390/rs12183062

Fu, W. J., Jiang, P. K., Zhou, G. M., & Zhao, K. L. (2014). Using Moran's I and GIS to study the spatial pattern of forest litter carbon density in a subtropical region of southeastern China. *Biogeosciences*, *11*(8), 2401–2409. https://doi.org/10.5194/bg-11-2401-2014

Gohain, K. J., Mohammad, P., & Goswami, A. (2021). Assessing the impact of land use land cover changes on land surface temperature over Pune city, India. *Quaternary International*, *575–576*, 259–269. https://doi.org/10.1016/j.quaint.2020.04.052

Guha, S., Govil, H., Gill, N., & Dey, A. (2020). Analytical study on the relationship between land surface temperature and land use/land cover indices. *Annals of GIS*, *26*(2), 201–216. https://doi.org/10.1080/19475683.2020.1754291

Horo, J. P., & Punia, M. (2019). Urban dynamics assessment of Ghaziabad as a suburb of National Capital Region, India. *GeoJournal*, *84*(3), 623–639. https://doi.org/10.1007/s10708-018-9877-0

Hu, X., Ma, C., Huang, P., & Guo, X. (2021). Ecological vulnerability assessment based on AHP-PSR method and analysis of its single parameter sensitivity and spatial autocorrelation for ecological protection – A case of Weifang City, China. *Ecological Indicators*, *125*, 107464. https://doi.org/10.1016/j.ecolind.2021.107464

Islam, S. M. S., Islam, K. M. A., & Mullick, M. R. A. (2022). Drought hot spot analysis using local indicators of spatial autocorrelation: An experience from Bangladesh. *Environmental Challenges*, *6*, 100410. https://doi.org/10.1016/J.ENVC.2021.100410

Kaiser, E. A., Rolim, S. B. A., Grondona, A. E. B., Hackmann, C. L., de Marsillac Linn, R., Käfer, P. S., da Rocha, N. S., & Diaz, L. R. (2022). Spatiotemporal Influences of LULC Changes on Land Surface Temperature in Rapid Urbanization Area by Using Landsat-TM and TIRS Images. *Atmosphere*, *13*(3), 460. https://doi.org/10.3390/atmos13030460

Kumari, M., Sarma, K., & Sharma, R. (2019). Using Moran's I and GIS to study the spatial pattern of land surface temperature in relation to land use/cover around a thermal power plant

in Singrauli district, Madhya Pradesh, India. *Remote Sensing Applications: Society and Environment*, *15*, 100239. https://doi.org/10.1016/j.rsase.2019.100239

Li, J., Zheng, X., Zhang, C., & Chen, Y. (2018). Impact of Land-Use and Land-Cover Change on Meteorology in the Beijing–Tianjin–Hebei Region from 1990 to 2010. *Sustainability*, *10*(2), 176. https://doi.org/10.3390/su10010176

Masson, V., Lemonsu, A., Hidalgo, J., & Voogt, J. (2020). Urban Climates and Climate Change. *Annual Review of Environment and Resources*, *45*(1), 411–444. https://doi.org/10.1146/annurev-environ-012320-083623

Moazzam, M. F. U., Doh, Y. H., & Lee, B. G. (2022). Impact of urbanization on land surface temperature and surface urban heat Island using optical remote sensing data: A case study of Jeju Island, Republic of Korea. *Building and Environment*, 109368. https://doi.org/10.1016/j.buildenv.2022.109368

Naikoo, M. W., Rihan, M., Ishtiaque, M., & Shahfahad. (2020). Analyses of land use land cover (LULC) change and built-up expansion in the suburb of a metropolitan city: Spatio-temporal analysis of Delhi NCR using landsat datasets. *Journal of Urban Management*, *9*(3), 347–359. https://doi.org/10.1016/j.jum.2020.05.004

Nations, U., of Economic, D., Affairs, S., & Division, P. (2019). World Urbanization Prospects: The 2018 Revision. In *World Urbanization Prospects: The 2018 Revision*. UN. https://doi.org/10.18356/b9e995fe-en

Park, Y., Kim, S. H., Kim, S. P., Ryu, J., Yi, J., Kim, J. Y., & Yoon, H. J. (2022). Spatial autocorrelation may bias the risk estimation: An application of eigenvector spatial filtering on the risk of air pollutant on asthma. *Science of the Total Environment*, *843*, 157053. https://doi.org/10.1016/j.scitotenv.2022.157053

Qu, L., Chen, Z., Li, M., Zhi, J., & Wang, H. (2021). Accuracy Improvements to Pixel-Based and Object-Based LULC Classification with Auxiliary Datasets from Google Earth Engine. *Remote Sensing*, *13*(3), 453. https://doi.org/10.3390/rs13030453

Rehman, A., Qin, J., Shafi, S., Khan, M. S., Ullah, S., Ahmad, K., Rehman, N. U., & Faheem, M. (2022). Modelling of Land Use/Cover and LST Variations by Using GIS and Remote Sensing: A Case Study of the Northern Pakhtunkhwa Mountainous Region, Pakistan. *Sensors*, *22*(13), 4965. https://doi.org/10.3390/s22134965

Rosado, R. M. G., Guzmán, E. M. A., Lopez, C. J. E., Molina, W. M., García, H. L. C., & Yedra, E. L. (2020). Mapping the LST (Land Surface Temperature) with Satellite Information and Software ArcGis. *IOP Conference Series: Materials Science and Engineering*, *811*(1), 012045. https://doi.org/10.1088/1757-899X/811/1/012045

Sarkar, R. (2020). Association of urbanisation with demographic dynamics in India. *GeoJournal*, *85*(3), 779–803. https://doi.org/10.1007/s10708-019-09988-y

Shaikh, S. F. E. A., See, S. C., Richards, D., Belcher, R. N., Grêt-Regamey, A., Galleguillos Torres, M., & Carrasco, L. R. (2021). Accounting for spatial autocorrelation is needed to avoid misidentifying trade-offs and bundles among ecosystem services. *Ecological Indicators*, *129*, 107992. https://doi.org/10.1016/J.ECOLIND.2021.107992

Stewart, S. B., & Nitschke, C. R. (2017). Improving temperature interpolation using MODIS LST and local topography: a comparison of methods in south east Australia. *International Journal of Climatology*, *37*(7), 3098–3110. https://doi.org/10.1002/joc.4902

Subasinghe, S., Estoque, R., & Murayama, Y. (2016). Spatiotemporal Analysis of Urban Growth Using GIS and Remote Sensing: A Case Study of the Colombo Metropolitan Area, Sri Lanka. *ISPRS International Journal of Geo-Information*, *5*(11), 197.

https://doi.org/10.3390/ijgi5110197

Tassi, A., & Vizzari, M. (2020). Object-Oriented LULC Classification in Google Earth Engine Combining SNIC, GLCM, and Machine Learning Algorithms. *Remote Sensing*, *12*(22), 3776. https://doi.org/10.3390/rs12223776

Yan, X., Feng, Y., Tong, X., Li, P., Zhou, Y., Wu, P., Xie, H., Jin, Y., Chen, P., Liu, S., Xv, X., Liu, S., & Wang, C. (2021). Reducing spatial autocorrelation in the dynamic simulation of urban growth using eigenvector spatial filtering. *International Journal of Applied Earth Observation and Geoinformation*, *102*, 102434. https://doi.org/10.1016/J.JAG.2021.102434.